JGR Space Physics

RESEARCH ARTICLE
10.1029/2023JA031758

Multiscale Observation of Magnetotail Reconnection Onset: 1. Macroscopic Dynamics

Kevin J. Genestreti[1], Charles J. Farrugia[2], San Lu[3,4], Sarah K. Vines[5], Patricia H. Reiff[6], Tai Phan[7], Daniel N. Baker[8], Trevor W. Leonard[8,9], James L. Burch[10], Samuel T. Bingham[5,†], Ian J. Cohen[5], Jason R. Shuster[11,12], Daniel J. Gershman[11], Christopher G. Mouikis[2], Anthony J. Rogers[2], Roy B. Torbert[1,2], Karlheinz J. Trattner[8], James M. Webster[6,10], Li-Jen Chen[11], Barbara L. Giles[11], Narges Ahmadi[7], Robert E. Ergun[7], Christopher T. Russell[3], Robert J. Strangeway[3], and Rumi Nakamura[13]

[1]Earth Oceans and Space, Southwest Research Institute, Durham, NH, USA, [2]Earth Oceans and Space, University of New Hampshire, Durham, NH, USA, [3]Institute for Geophysics and Planetary Physics, University of California Los Angeles, Los Angeles, CA, USA, [4]Now at School of Earth and Space Sciences, University of Science and Technology of China, Hefei, China, [5]Applied Physics Laboratory, Johns Hopkins University, Laurel, MD, USA, [6]Rice Space Institute, Rice University, Houston, TX, USA, [7]Space Science Laboratory, University of California Berkeley, Berkeley, CA, USA, [8]Laboratory for Atmospheric and Space Physics, University of Colorado Boulder, Boulder, CO, USA, [9]Now at Cooperative Institute for Research in Environmental Sciences, National Oceanic and Atmospheric Administration National Centers for Environmental Information, University of Colorado Boulder, Boulder, CO, USA, [10]Space Science and Engineering Division, Southwest Research Institute, San Antonio, TX, USA, [11]Goddard Space Flight Center, National Aeronautics and Space Administration, Greenbelt, MD, USA, [12]Now at Space Science Center, Institute for the Study of Earth Oceans and Space, University of New Hampshire, Durham, NH, USA, [13]Space Research Institute, Austrian Academy of Sciences, Graz, Austria

[†]Deceased.

Key Points:

- Magnetotail reconnection onset was observed during a fortuitous multiscale conjunction of the heliophysics observatories
- A transient solar wind pressure pulse triggered thinning and stretching of the cross-tail current sheet without significant flux loading
- A second solar wind pressure pulse caused the thinned current sheet to rapidly collapse and reconnect

Correspondence to:

K. J. Genestreti,
kevin.genestreti@swri.org

Citation:

Genestreti, K. J., Farrugia, C. J., Lu, S., Vines, S. K., Reiff, P. H., Phan, T., et al. (2023). Multiscale observation of magnetotail reconnection onset: 1. Macroscopic dynamics. *Journal of Geophysical Research: Space Physics*, *128*, e2023JA031758. https://doi.org/10.1029/2023JA031758

Received 7 JUN 2023
Accepted 19 OCT 2023

Abstract We analyze a magnetotail reconnection onset event on 3 July 2017 that was observed under otherwise quiescent magnetospheric conditions by a fortuitous conjunction of six space and ground-based observatories. The study investigates the large-scale coupling of the solar wind–magnetosphere system that precipitated the onset of the magnetotail reconnection, focusing on the processes that thinned and stretched the cross-tail current layer in the absence of significant flux loading during a 2-hr-long preconditioning phase. It is demonstrated with data in the (a) upstream solar wind, (b) at the low-latitude magnetopause, (c) in the high-latitude polar cap, and (d) in the magnetotail that the typical picture of solar wind-driven current sheet thinning via flux loading does not appear relevant for this particular event. We find that the current sheet thinning was, instead, initiated by a transient solar wind pressure pulse and that the current sheet thinning continued even as the magnetotail and solar wind pressures decreased. We suggest that field line curvature-induced scattering (observed by magnetospheric multiscale) and precipitation (observed by Defense Meteorological Satellite Program) of high-energy thermal protons may have evacuated plasma sheet thermal energy, which may require a thinning of the plasma sheet to preserve pressure equilibrium with the solar wind.

1. Introduction

Magnetospheric substorms are triggered by magnetotail reconnection, which, in turn, follows thinning and stretching of the cross-tail current sheet (Hones, 1979). The commonly accepted processes that thin and stretch the current sheet require solar wind driving of the magnetosphere with southward interplanetary magnetic fields (IMF) $B_Z \lesssim 0$ (Baker et al., 1996). Magnetic reconnection between the IMF and low-latitude dayside magnetopause "opens" magnetospheric field lines that are then convected over the geomagnetic poles into the high-latitude magnetotail lobes (Dungey, 1961). Magnetic flux loading causes the tail lobes to flare outward at a larger angle, intruding further into the solar wind ram flow (McPherron & Hsu, 2002). For steady solar wind dynamic pressure, the tail pressure must increase to maintain equilibrium, which results in compression of the equatorial tail current sheet. Simultaneously, large-scale pressure gradients drive a return flow of high-entropy flux tubes from the near-Earth equatorial tail back to the magnetopause that is eroded by dayside reconnection (Hsieh & Otto, 2015). Again, the thickness of the equatorial current layer is reduced to maintain vertical pressure balance. Magnetotail reconnection is common during northward IMF too (Zhang et al., 2016), and the mechanisms that drive current sheet thinning and stretching without low-latitude dayside reconnection are not understood.

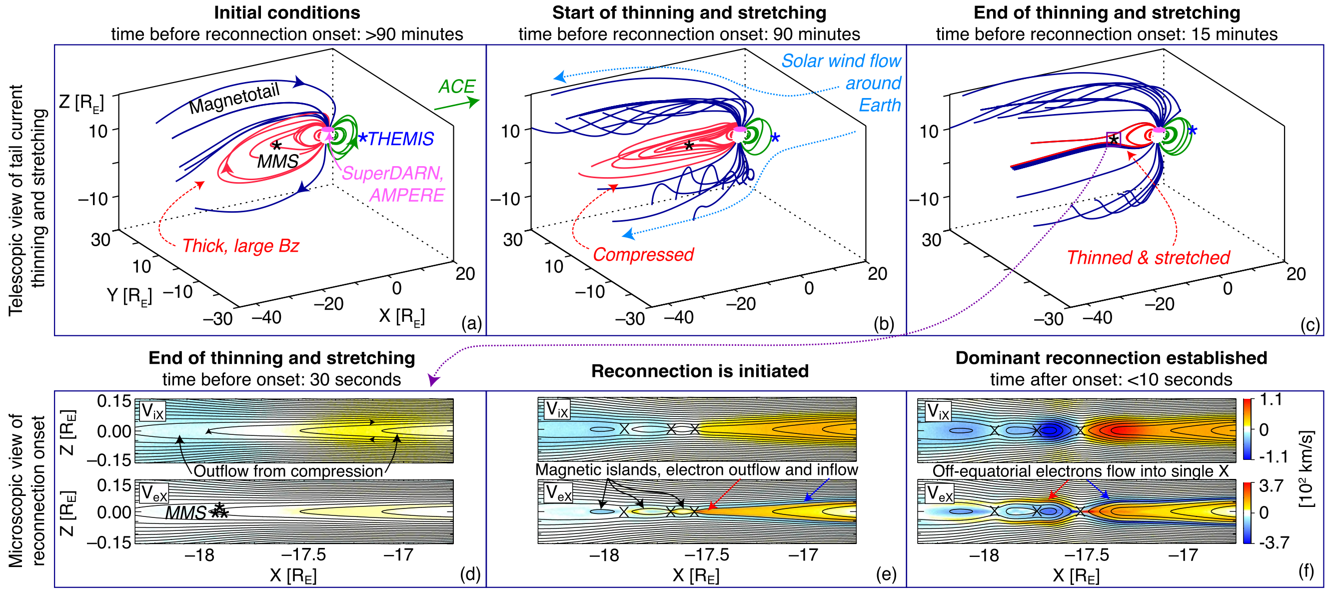

Figure 1. (Top) Large-scale and (bottom) small-scale physics of magnetotail reconnection onset, illustrated by (top) a global MHD and (bottom) a fully kinetic 2.5-D PIC simulation. (a and d) illustrate the coverage of our multiscale constellation of observatories. This paper focuses on the macro-scale dynamics while the companion focuses on the microscale physics. The axes in (a–c) correspond to geocentric solar magnetic coordinates, while those in (d–f) are arbitrary coordinates locally normal and tangential to the tail current sheet. Times in (a–c) are relative to the reconnection onset time observed by magnetospheric multiscale at 5:23 UT. Times in (d–f) are relative to the onset of reconnection in the PIC simulation.

Isotropic proton precipitation in the high-latitude ionosphere is a well-known symptom of cross-tail current sheet thinning (Donovan et al., 2012; Sergeev et al., 1983). As the tail current sheet thins down to the proton-kinetic scale, nonadiabatic scattering drives pitch angle diffusion in previously trapped current sheet protons. Protons that become sufficiently field aligned stream out of the current sheet and into ionosphere and neutral atmosphere, where they are effectively lost from the tail. This pitch angle scattering is most efficient when particles' gyroradii $R_G(E_\perp)$ are comparable to the magnetic field line curvature (FLC) radii R_C in the central current sheet; theoretical works consider a critical range of $1 \lesssim \kappa\left(=\sqrt{R_C/R_G}\right) \lesssim 3$ (Büchner & Zelenyi, 1987, 1989; Delcourt et al., 1996; Sergeev et al., 1983). Thus, FLC pitch angle scattering acts like a bandpass filter that ejects protons most efficiently over a range of perpendicular energies $E_\perp$, and as a thick ($R_C >> R_G$) current sheet thins, FLC scattering acts most efficiently on lower and lower energy protons. Field line entropy $pV^{5/3}$ (where p is the pressure and V is the volume of a flux tube element, as in Birn et al. , 2009, Equation 4) is typically assumed to be conserved without reconnection (Birn et al., 2009) and, since FLC scattering will reduce the plasma sheet thermal energy in the absence of refilling, lossy FLC scattering and current sheet deformation and/or thinning may go hand-in-hand.

In this study, we analyze a fortuitous conjunction of six spacecraft and ground-based observatories, which occurred on 3 July 2017, to determine the global causes of one magnetotail reconnection event. An overview of the regions covered by spacecraft and ground-based observatories is provided in Figure 1a, and a summary of the key observations follows. The magnetotail current sheet was initially thick, more dipolar, and stable (Section 3.1). The IMF B_Z was weak or strongly positive, and low-latitude dayside reconnection was expected to be weak or fully disabled based on the atypically large plasma β observed in the magnetosheath and low magnetic shear at the magnetopause (Section 3.2). Observed patterns in the global field-aligned current (FAC) system indicated a preference for magnetopause reconnection poleward of the cusps (often referred to as high-latitude reconnection), which does not supply energy to the high-latitude tail or erode the low-latitude dayside. Ionospheric observations showed weak convection in the polar cap that was, at times, either weakly antisunward (indicative of weak magnetotail loading by low-latitude dayside reconnection) or sunward (indicating the predominance of reconnection poleward of the magnetopause cusps). The polar cap boundary moved equator-ward by ~1° prior to reconnection onset, which is a signature of open-flux loading (Section 3.3). These data are somewhat consistent with a global magnetospheric simulation of the event, which predicts weak ionospheric convection but a larger ~5° expansion of the polar cap (Section 3.4). Despite the lack of significant evidence for solar wind driving, the magnetotail current sheet thinned and stretched substantially (Section 3.5) until the impact of a (second) solar wind pressure pulse precipitated the collapse of the current sheet down to electron scales and reconnection onset (Section 3.6). We note that the tail pressure decreased during the thinning phase and magnetic flux erosion. We conclude that the thinning may have been driven by proton FLC scattering, which was observed in situ in the plasma sheet and also at the ionospheric foot point. A companion paper (hereafter paper 2) focuses on the microphysics observed by magnetospheric multiscale (MMS) during the reconnection onset.

This paper is organized as follows: in the next section, we provide brief overviews of our data set, analysis techniques, empirical models, and physics-based simulation. For brevity, we provide citations with more rigorous descriptions of the instrumentation, data sets, and models. In Section 3, we analyze the data and compare it with our simulation. Finally, in Section 4, we discuss the implications of our findings within the context of the standard picture of substorms. We stress the need for future modeling and data collection endeavors to confirm or refute the findings that were made here, which interpret the multiscale physics of our sparsely covered magnetosphere.

2. Data, Analysis Methods, and Models

2.1. Data and Analysis Methods

The Advanced Composition Explorer (ACE) spacecraft orbits the Earth-sun L1 point and provides in situ measurements of the upstream solar wind plasma. Data are obtained from the OMNI database and are (a) propagated to Earth's bow shock and (b) available at a cadence of 1 per min.

The Time History of Events and Macroscopic Interactions during Substorms (THEMIS) mission (Angelopoulos, 2008) provides our study with two-point in situ measurements of the low-latitude, dusk-side magnetopause. Plasma and magnetic field data from THEMIS satellites D and E are used to (a) obtain the plasma conditions in the shocked solar wind upstream of the magnetopause, (b) identify THEMIS magnetopause crossings, and (c) monitor for signatures of low-latitude reconnection, specifically Alfvénic plasma jets at the magnetopause. THEMIS-D, which was located at $[XYZ]_{GSM} = [6.8, 8.7, -2.6]$ R_E on 3 July 2017 at 4:00 UT, was located in the magnetosheath for most of the event. THEMIS-E, which was closer to Earth than THEMIS-D ($[XYZ]_{GSM} = [6.8, 3.6, -3.3]$ R_E on 3 July 2017 at 4:00 UT), was located in the magnetosphere during most of the event. However, both spacecraft fully and/or partially crossed the magnetopause multiple times. For THEMIS-D, magnetopause crossings occurred near the tail reconnection onset time (~5:20 UT) on the inbound leg of its orbit. For THEMIS-E, magnetopause crossings occurred after the impacts of the solar wind pressure pulses, which compressed the magnetopause down to the spacecraft location. Plasma particle fluid moments and omnidirectional fluxes are available once every 4.2 s. Magnetic field vector measurements are available once every 62.5 ms. When necessary, simple boxcar averaging is used to downsample the magnetic field to the plasma particle data cadence.

The Active Magnetosphere and Planetary Electrodynamics Response (AMPERE) mission is a constellation of 66 low-altitude satellites, which provides this study with a "remote" view of the global magnetospheric current system by measuring, in situ, multi-point magnetic perturbations. These AMPERE magnetic field data are used to derive the global FAC configuration at high northern latitudes. FACs indicate magnetospheric magnetic stresses, which can be generated by, among other processes, magnetic reconnection at the magnetopause and magnetotail. Snapshots of the FACs are accumulated over the course of 10 min, are available at 1 snapshot per 10 min, and are accumulated by no fewer than 11 spacecraft. The sensitivity of the magnetometers is such that currents below 0.075 μA/m^2 are understood to be indiscernible from noise. Currents below this threshold are discarded in this study.

The Super Dual Auroral Radar Network (SuperDARN) is a network of ground-based high-frequency radar stations, which provides this study with a remote view of the northern polar cap (PCN) area and convection electric field, which are derived from maps of plasma convection. The motion of the polar cap boundary indicates whether opened magnetic field lines are being accumulated (polar cap area growth) or closed (polar cap area reduction). The Heppner-Maynard convection boundary (Heppner & Maynard, 1987), a proxy for the open-closed field line boundary, is located at the lowest latitude in which no fewer than three radars measure a line-of-sight velocity of 100 m/s along the zero-potential contour of the polar cap electric field (Imber et al., 2013). (Note: the convection boundary could not be derived reliably from AMPERE data as the FACs were too weak to provide robust fits.) The cross-polar-cap potential is the total potential drop across the polar cap area, and is used as an indicator of the amount of polar ionospheric convection.

MMS is a constellation of four very-closely-spaced satellites that provide the study with in situ, high-spatiotemporal-resolution measurements of the plasma particles and electric and magnetic fields (Burch et al., 2016). During this event, on 3 July 2017 at 5:20 UT, MMS was at $X_{\mathrm{GSM}} = -17\ R_E$ and $Y_{\mathrm{GSM}} = 3\ R_E$. MMS-1, 2, and 3, separated by 26 km, effectively provide this study with a point measurement of the larger magnetotail dynamics. For this event, no data was available from MMS-4. When unspecified, plots or analyses of "MMS data" use averaged data from these three satellites. The plasma ion and electron fluid moments from the fast plasma investigation (FPI) sensors (Pollock et al., 2016) are used to determine the cross-tail current density as $J_y = en_i(v_{iy} - v_{ey})$. The magnetic field, FPI ion and electron data, and energetic ion spectrometer (Mauk et al., 2016) data are used to find the total magnetohydrodynamic pressure. Magnetic field data from the fluxgate magnetometers are determined to within a precision of ≤0.1 nT per component (Torbert et al., 2016). Magnetic field and plasma fluid moments are used to determine the time-dependent half-thickness of the cross-tail current sheet via the Harris approximation, $h(t) = \left(B_0^2(t) - B_x^2(t)\right)/\mu_0 B_0(t) J_y(t)$ (Thompson et al., 2005). Here, B_0 is the magnetic field strength in the plasma sheet boundary layer, approximated as 60% of the lobe magnetic field strength or $B_0 = 0.6 B_{lobe} = 0.6\sqrt{B^2 + \mu_0 P_{therm}}$, where P_{therm} is the particle thermal pressure. The fraction $B_0/B_{\mathrm{lobe}} = 0.6$ was chosen to match observations of the plasma sheet boundary when it is first observed during interval of current sheet flapping on 3 July 2017 5:23 UT. The 60% is slightly larger than the typical range of $0.3 \lesssim B_0/B_{\mathrm{lobe}} \lesssim 0.5$ (Petrukovich et al., 2015). For reference, we also calculate the half-thickness using $B_0/B_{\mathrm{lobe}} = 1$, as in Thompson et al. (2005), which is relevant when a thin current sheet is not embedded within the thicker plasma sheet. Prior to calculating h, long (10 min) time averaging is performed to reduce noise in the initially very weak J_y. Ion fluxes from FPI were combined with proton fluxes from the energetic ion spectrometer to determine the scalar ion thermal pressure and total MHD pressure (Figures 2n and 6f–6g). Whenever necessary, the magnetic field data are resampled at the plasma particle cadence via boxcar averaging. In this study, survey-rate data are used, meaning the plasma particle and magnetic field data are obtained at cadences of once per 4.5 s and 8 per s, respectively.

Defense Meteorological Satellite Program (DMSP) is a constellation of low-altitude satellites that collects space weather data, including ions and electron fluxes at approximately 850 km altitude. For the event studied here, two passes of DMSP F-16 came very near the modeled footprint of MMS. DMSP F-16 particle flux data are used to qualitatively evaluate whether plasma sheet particles near MMS may be lost to the ionosphere.

The Synchronous Orbit Particle Analyzer (SOPA) instruments onboard the geosynchronous-orbiting Los Alamos Nation Laboratory GEO satellites measure energetic ion (50 keV to 50 MeV) and electron (50 keV to ≥1.5 MeV) fluxes. These data were used to look for particle injections into the near-midnight inner magnetosphere driven by the Earthward-propagating jets from magnetotail reconnection. The methodology used was straightforward; data taken near midnight were scanned at/near the time MMS observed reconnection signatures. Dispersed or dispersionless injections are identified as gradual or steep enhancements in the fluxes of energetic particles in energy-time-flux diagrams (Sarris et al., 1976). No such signatures were identified, indicating that the Earthward jets from the reconnection did not penetrate into geosynchronous orbit. No SOPA data are shown.

2.2. Empirical Models and Indices

We use the T96 empirical model to trace magnetospheric field lines (Tsyganenko, 1995, 1996). Field-line tracing is used to (a) estimate the outer-magnetospheric source region of the FACs observed by AMPERE and (b) estimate the proximity between DMSP and the ionospheric foot points of magnetotail field lines near MMS.

We use the empirical maximum magnetic shear model (Trattner et al., 2007) to estimate the location of the magnetopause reconnection region relative to THEMIS and estimate the outflow direction expected for any THEMIS-observed reconnection outflows. The maximum shear model uses the cooling empirical model (Cooling et al., 2001) for the IMF draping about the T96 magnetopause. The location of the reconnection line is determined as the line of maximum sheared magnetic energy. The shear model is also used to estimate the magnetic shear angle at the subsolar magnetopause.

We use the empirically derived Boyle index (Boyle et al., 1997) to estimate the cross-polar-cap potential from ACE solar wind data, which is found to be in good agreement with SuperDARN-derived values. We use the PCN index as a proxy for the strength of convection in the polar ionosphere (Troshichev et al., 1988). Future work is needed to compare SuperDARN convection maps with the PCN and magnetosphere-ionosphere simulation. We used the ϵ parameter to approximate the energy input rate (from the solar wind into the magnetosphere via dayside

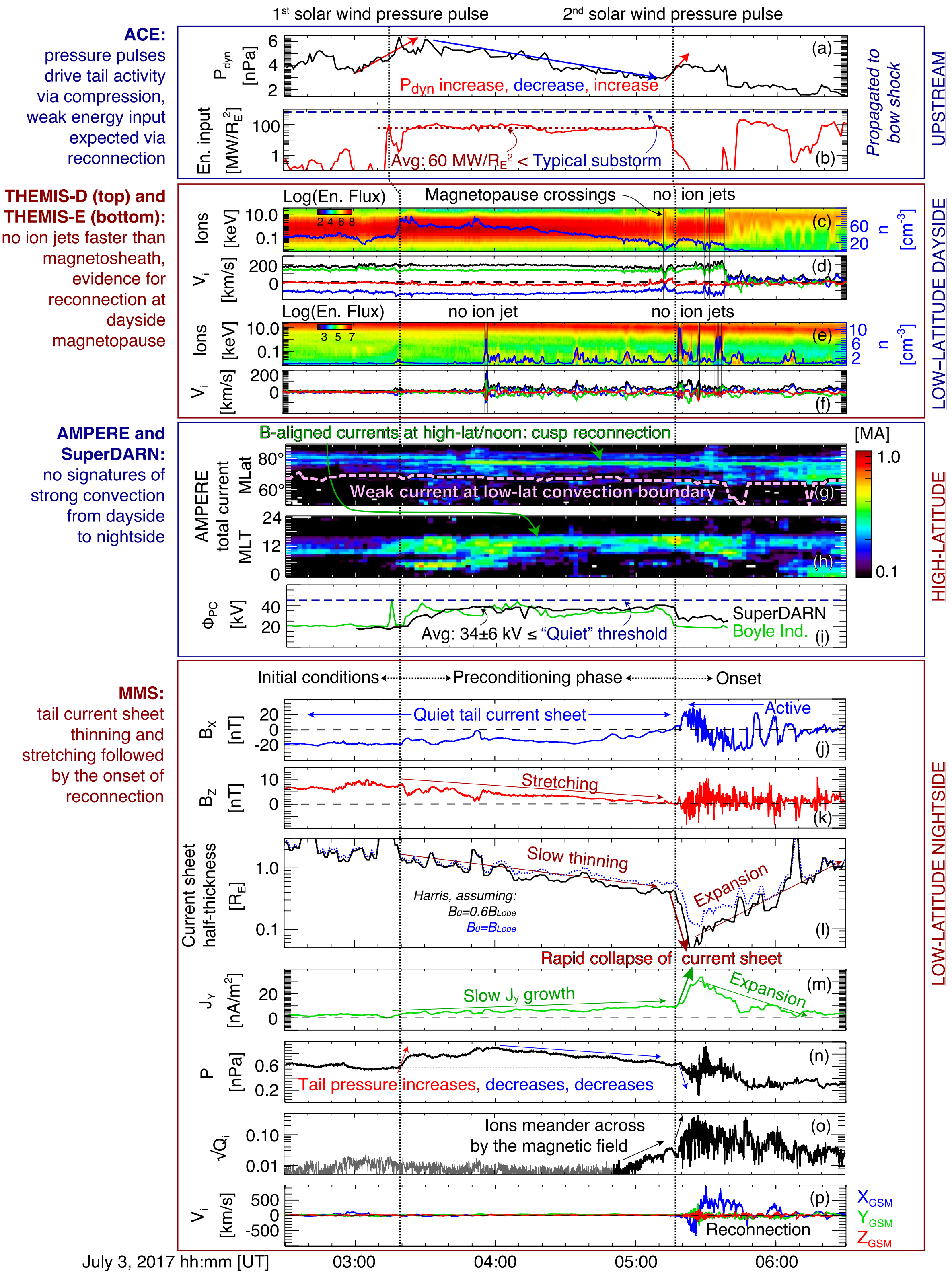
1st solar wind pressure pulse
2nd solar wind pressure pulse
ACE:
pressure pulses drive tail activity via compression, weak energy input expected via reconnection
P_dyn [nPa]
6
4
2
(a)
P_dyn increase, decrease, increase
En. input [MW/R_E^2]
100
1
Avg: 60 MW/R_E^2 < Typical substorm
(b)
Propagated to bow shock
UPSTREAM
THEMIS-D (top) and THEMIS-E (bottom):
no ion jets faster than magnetosheath, evidence for reconnection at dayside magnetopause
Log(En. Flux)
2 4 6 8
Magnetopause crossings
no ion jets
Ions [keV]
10.0
0.1
(c)
60
20
n [cm^-3]
V_i [km/s]
200
0
(d)
Log(En. Flux)
3 5 7
no ion jet
no ion jets
10.0
0.1
(e)
10
6
2
200
0
(f)
LOW-LATITUDE DAYSIDE
AMPERE and SuperDARN:
no signatures of strong convection from dayside to nightside
B-aligned currents at high-lat/noon: cusp reconnection
AMPERE total current
MLat
80°
60°
Weak current at low-lat convection boundary
(g)
MLT
24
12
0
(h)
[MA]
1.0
0.1
Φ_PC [kV]
40
20
SuperDARN
Boyle Ind.
Avg: 34±6 kV ≤ "Quiet" threshold
(i)
HIGH-LATITUDE
MMS:
tail current sheet thinning and stretching followed by the onset of reconnection
Initial conditions
Preconditioning phase
Onset
B_X [nT]
20
0
-20
Quiet tail current sheet
Active
(j)
B_Z [nT]
10
0
Stretching
(k)
Current sheet half-thickness [R_E]
1.0
0.1
Slow thinning
Harris, assuming:
B0=0.6B_Lobe
B0=B_Lobe
Expansion
(l)
Rapid collapse of current sheet
J_Y [nA/m^2]
20
0
Slow J_y growth
Expansion
(m)
P [nPa]
0.6
0.2
Tail pressure increases, decreases, decreases
(n)
√Q_i
0.10
0.01
Ions meander across by the magnetic field
(o)
V_i [km/s]
500
0
-500
Reconnection
(p)
X_GSM
Y_GSM
Z_GSM
LOW-LATITUDE NIGHTSIDE
July 3, 2017 hh:mm [UT]
03:00
04:00
05:00
06:00

Figure 2.

reconnection) per-unit-magnetopause-area, where $\epsilon = V_{SW} B_{SW}^2 / \mu_0 \sin^4(\theta/2)$ (Perreault & Akasofu, 1978) and θ is the clock angle of the IMF in the $Y - Z_{\mathrm{GSM}}$ plane.

2.3. Physics-Based Simulations

We use the Space Weather Modeling Framework/Block-Adaptive-Tree-Solarwind-Roe-Upwind-Scheme model (Tóth et al., 2012) to simulate the global magnetospheric-ionospheric dynamics during 3 July 2017 from midnight to 8:00 UT. The real time-dependent dipole tilt angle is used. Upstream solar wind conditions are obtained from ACE via the OMNI database. The high-resolution grid with >9.6 million cells was used. The modeled ionospheric conductance was determined self-consistently by geomagnetic FACs. The model is used to (a) provide qualitative visualizations of the magnetospheric configuration (e.g., Figure 1) and (b) compare with low-altitude and ionospheric observations by AMPERE spacecraft and SuperDARN radars. The full inputs and outputs of our model run are publicly available on the Community Coordinated Modeling Center.

The particle-in-cell simulation shown in Figures 1d–1f was performed using the same fully kinetic 2.5-d code as in Lu et al. (2020, 2022). The initial conditions were chosen to roughly correspond to those observed by MMS near the time of reconnection onset. The initial current sheet had a finite B_Z. Reconnection was initiated by applying a brief pulse of the electric field E_Y to the regions upstream of the current sheet early in the run. The pulse in E_Y imitates the solar wind-driven compression of the high-latitude magnetosphere. Selected frames from the run, shown in Figures 1d and 1e, are used to illustrate the general dynamics of reconnection onset, and no detailed analysis or comparison with MMS is performed.

3. Data and Model Analyses

The event, which occurred on 3 July 2017, is described in terms of three phases, labeled (between Figures 2i and 2j) and demarcated by two vertical dashed lines ~3:19 and ~5:18 UT. The phases are (a) initial conditions, (b) preconditioning, and (c) reconnection onset, which describe the characteristic processes occurring in the magnetotail. The preconditioning phase is characterized by slow current sheet thinning (Figure 2l) and stretching (Figure 2k).

3.1. The Initially Quiet and Stable Tail

The initial state of the tail is shown in Figures 2j–2p to the left of the first vertical dashed line, that is, before 3:20 UT. The orientation of the geocentric solar magnetic (GSM) coordinate axes relative to the magnetosphere are shown in Figure 1a. The northward component of the equatorial magnetic field ($B_z \approx 5 - to - 10$ nT, Figure 2k) magnetizes ions and electrons. The thick current sheet ($h \approx 1$–$2\ R_E$, Figure 2l) does not enable the bulk ion population to meander across field lines, as is further evidenced by the negligible ion pressure nongyrotropy ($\sqrt{Q_i} \lesssim 1\%$, Figure 2o). Reconnection, which requires slippage of magnetic fields through plasma particles, is neither expected nor observed in this initial tail configuration.

3.2. Solar Wind Drivers During Preconditioning

The "inciting incident" was a transient ~50% increase in the solar wind dynamic pressure $\Delta P_{\mathrm{dyn},1}$ (first dashed vertical line, Figure 2a). $\Delta P_{\mathrm{dyn},1}$ corresponded to a pulsed increase in the solar wind (Figure 3a) and magnetosheath (blue line, Figure 2c) densities, and a significant compression of the magnetopause inward to near the location of THEMIS-E at $[X, Y, Z]_{GSM} = [6.8, 3.6, -3.3]\ R_E$ (first set of solid vertical lines, Figure 2e). After $\Delta P_{\mathrm{dyn},1}$, the solar wind energy input was elevated, but remained lower than the typical rate for a substorm (Akasofu, 1981) by roughly an order of magnitude (Figure 2b). The rise in the energy input rate corresponded to a rotation of the IMF from mostly northward to mostly duskward (Figure 3b).

Figure 2. (a) Solar wind dynamic pressure, (b) derived solar wind energy input, ϵ (see Section 2.2), (c) Time History of Events and Macroscopic Interactions during Substorms (THEMIS)-D ion energy flux (color) and density (blue line), (d) THEMIS-D ion bulk flow velocity, (e and f) are the same as (c and d), respectively, but for THEMIS-E, (g–h) Active Magnetosphere and Planetary Electrodynamics Response (AMPERE) total current as a function of MLat and magnetic local time (MLT) (respectively), integrated over (g) MLT and (h) magnetic latitude (MLat), where the pink line is the Heppner-Maynard boundary, (i) cross-polar-cap potential from Super Dual Auroral Radar Network (SuperDARN) (black) and the Boyle index (green), (j–k) MMS-observed B_X and B_Z, respectively, (l) the cross-tail current sheet thickness approximated for boundary conditions of 60% (black) and 100% (blue) of the lobe magnetic field, (m–p) magnetospheric multiscale (MMS)-observed cross-tail current density (m), total MHD pressure (n), ion nongyrotropy (o), and ion bulk flow vector (p). Two vertical dashed lines delineate the phases of magnetotail activity labeled above (j). The vertical lines jog rightward between panels (b and c) to account for small timing differences between the solar wind drivers (a–b) and their observed impacts on the magnetosphere (c–p).

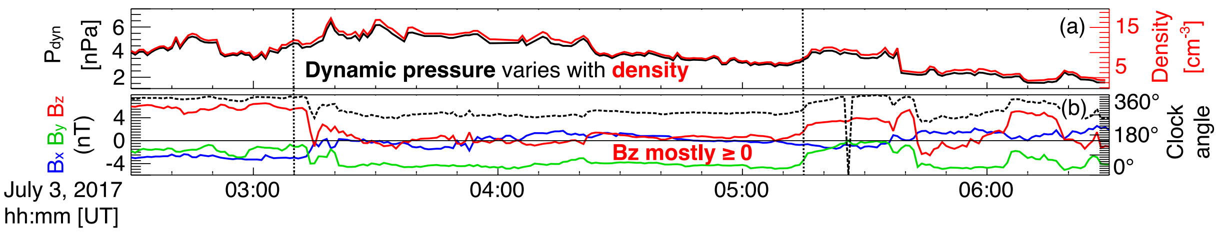

Figure 3. (a) Solar wind pressure (black) and density (red), (b) magnetic field vector in Geocentric Solar Magnetic (solid) and clock angle (dashed).

THEMIS-E partially crossed the magnetopause at 3:56 UT, between the first and second pressure pulses ($\Delta P_{\mathrm{dyn},1}$ and $\Delta P_{\mathrm{dyn},2}$, respectively). No clear reconnection jets were observed during the crossings (first set of vertical lines, Figures 2e and 2f). Strong and bipolar ion flows observed during the partial crossing indicate the fast inward-then-outward motion of the magnetopause during compression. THEMIS-D partially crossed the magnetopause twice at 5:11 and 5:15 UT (vertical lines in Figures 2c and 2d). Dayside reconnection exhausts were not observed during these THEMIS-D crossings.

Low-latitude reconnection is suppressed by large plasma β gradients and low magnetic shear across the magnetopause (Phan et al., 2013; Swisdak et al., 2003). The suppressed/enabled regimes of reconnection are often depicted as in Figure 4b, where reconnection is suppressed (enabled) in the region below (above) a rectifier curve defined by $\Delta\beta = L/d_i \tan(\theta/2)$, where L is the magnetopause thickness, and d_i is the ion inertial length. During the preconditioning phase (between the two vertical dashed lines in Figure 2e), the expected magnetic shear was roughly 80° at subsolar magnetopause and ~60°-to-110° near the THEMIS-D location (Figure 4a). THEMIS-E did not fully cross the magnetopause during the period shown in Figure 2 and the magnetosheath conditions near THEMIS-E cannot be determined. The plasma β observed by THEMIS-D in the high-density magnetosheath was initially $\beta \approx 400$ at the time of the solar wind pressure pulse impact following the arrival of the density enhancement in observed by ACE (Figure 3a), and it remained $\beta \geq 100$ until roughly 5:00 UT. THEMIS-D remained in the magnetosheath and magnetosphere boundary layer until after 6:00 UT, meaning that $\Delta\beta$ could not be calculated for each partial magnetopause crossing. Once in the magnetosphere, however, THEMIS-D observed $\beta = 0.4$, which is used with the time-dependent magnetosheath β to calculate $\Delta\beta$ (note that since the

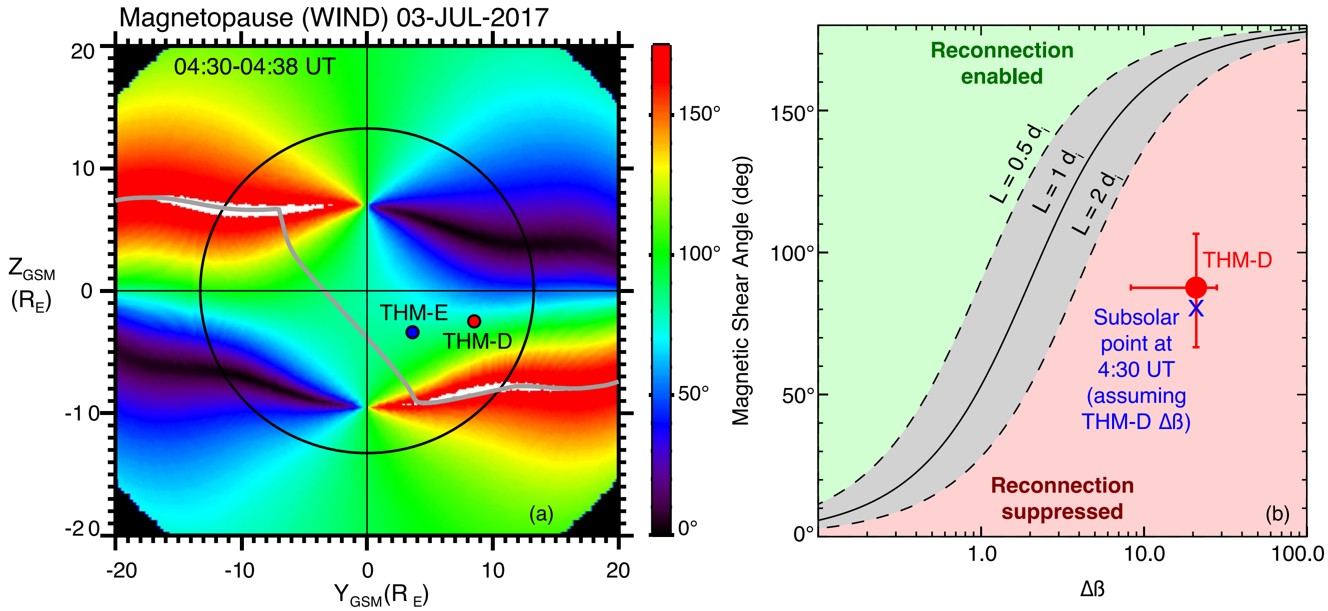

Figure 4. (a) The magnetopause magnetic shear angle (color) and X-line location (gray line) predicted by the maximum magnetic shear model, projected into the $Y_{\mathrm{GSM}} - Z_{\mathrm{GSM}}$ plane. The location of the terminator is marked with a black circle. (b) The average (red circle) and full range (red lines) of $\Delta\beta$ magnetic shear angles observed by Time History of Events and Macroscopic Interactions during Substorms (THEMIS)-D at the magnetopause during preconditioning, where time-varying magnetosheath and average magnetospheric values are used. Magnetospheric β and $\vec{B}$ are determined from THEMIS-D at 6:30–6:45 UT. Equivalent values for the subsolar point (blue X) at 4:30 UT are shown, where the modeled shear angle and THEMIS-observed $\Delta\beta$ are used.

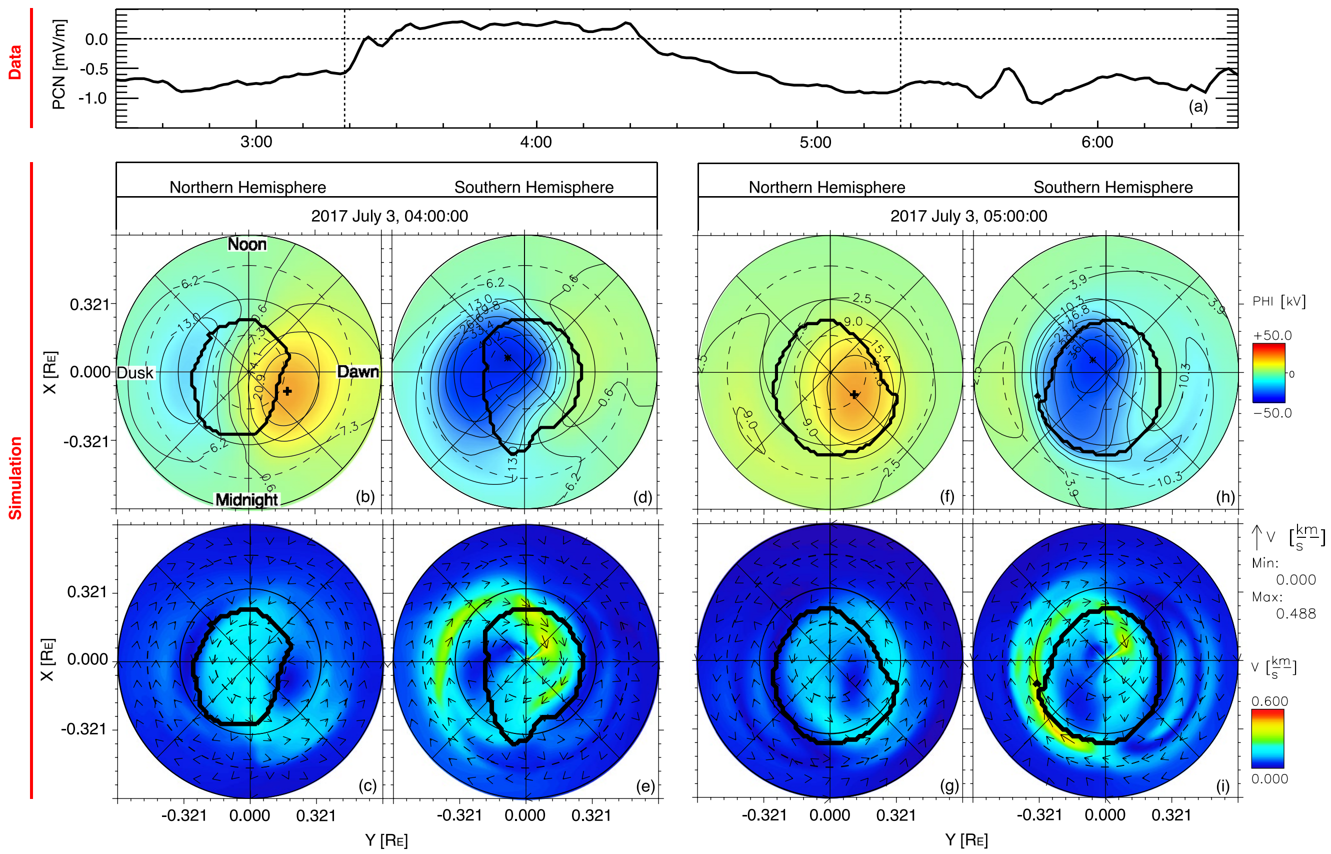

Figure 5. (a) The northern polar cap index from data (i.e., not from the simulation). (b–i) Simulated polar cap dynamics during the (b–e) early and (f–i) late stages of the preconditioning phase for the (b–c and f–g) northern and (d–e and h–i) southern polar cap. The top row shows the electric potential in color and contours. The bottom row shows the speed (colors) and velocity vector (arrows). The thick black lines indicate the polar cap boundaries.

magnetospheric β is typically small, $\Delta\beta$ is dominated by the magnetosheath β). The magnetic shear angle and $\Delta\beta$ indicate that low-latitude reconnection was likely suppressed at the THEMIS-D location, and possibly at the subsolar point, in the $\sim$2 hr after the impact of the solar wind pulse (Figure 4b).

3.3. Polar Cap During Preconditioning: Data

During the preconditioning phase (between the vertical dashed lines, Figure 2), the strongest FACs were observed by AMPERE at high magnetic latitudes (Figure 2g) at postnoon magnetic local time (Figure 2h). Field lines in this region are open and map to the high-latitude magnetopause poleward of the cusp. The dusk-ward skew of the FACs is consistent with high-latitude reconnection for strong IMF $B_y < 0$ (Burch et al., 1985). High-latitude, open-field-line reconnection does not drive day-to-night flux transport, though it enables the penetration of the IMF B_y into the lobes, which can torque and twist the cross-tail current sheet (Crooker, 1979; Tsyganenko & Sitnov, 2007).

Much weaker currents are observed near the low-latitude Heppner-Maynard convection boundary (Figure 2g, dashed pink line). These lower-latitude currents are near the pre-noon open-closed field line boundary, and may indicate weak reconnection of closed field lines. The latitude of the strongest FACs did not move appreciably either poleward or equator-ward after 3:43 UT, which indicates that the magnetopause was not being eroded by closed-field-line reconnection (Coxon et al., 2014). The PCN index PCN suggests that weak antisunward convection occurred during and shortly after $\Delta P_{\mathrm{dyn},1}$, while reverse convection occurred at all other times studied here (Figure 5a). Further analysis of SuperDARN convection maps is needed to verify this picture. Both the PCN and cross-polar-cap potential (see Figure 2i) were weak, with the latter being within the "quiescent" threshold of Oliver et al. (1983). The observed cross-polar-cap potential (black line Figure 2i) is in excellent agreement with the empirically modeled approximation (green line Figure 2i) (Boyle et al., 1997).

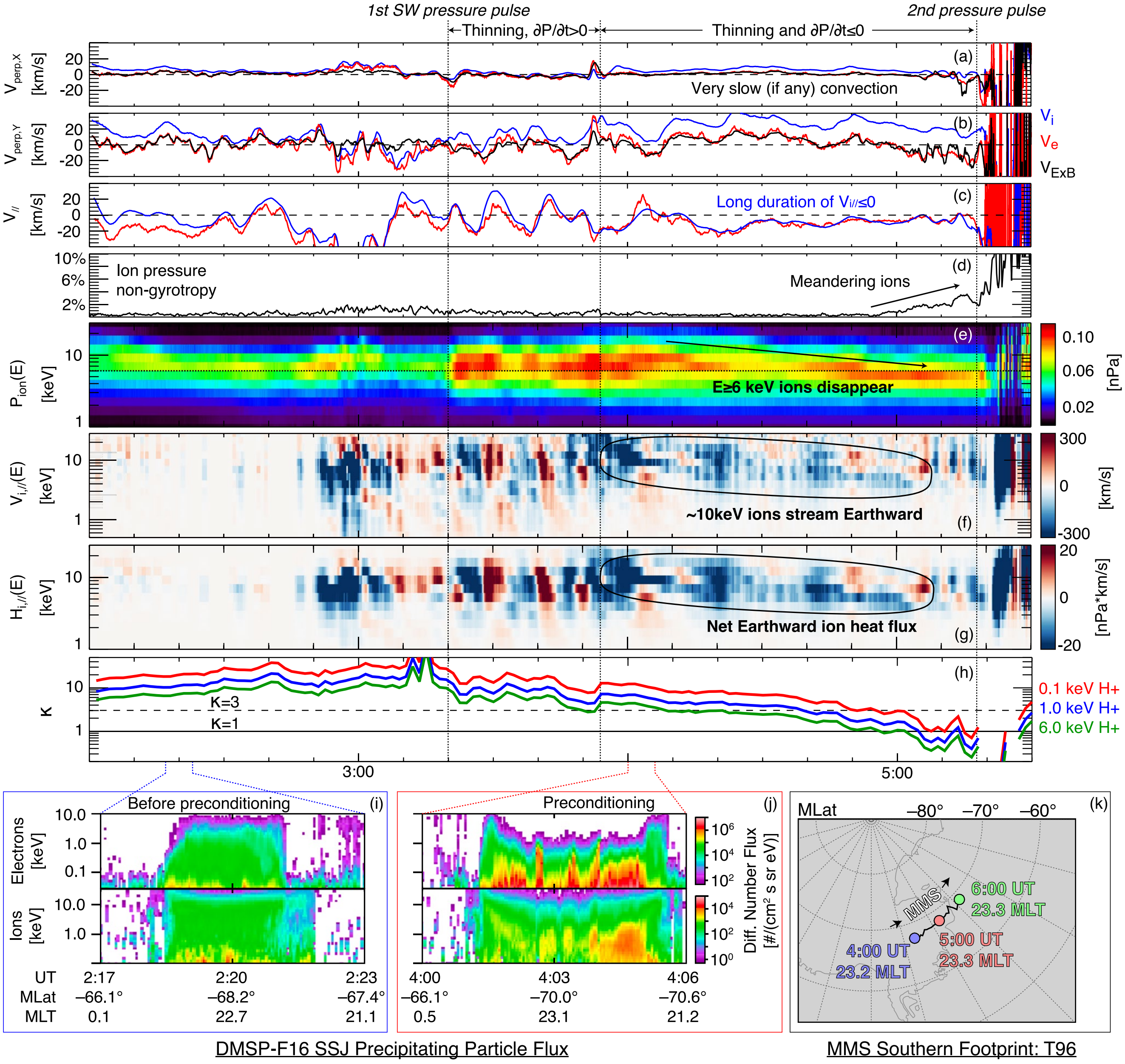

Figure 6. (a–b): The X_{GSM} and Y_{GSM} components of the perpendicular (blue) ion, (red) electron, and $E \times B$ velocities. (c): The parallel velocities, with the same color code as (a and b). (d): Ion nongyrotropy from the $\sqrt{Q}$ parameter. (e–g): The partial-energy ion scalar pressure (i.e., scalar pressure per energy bin), parallel ion velocity, and parallel ion heat flux, respectively. (h): The ion adiabaticity parameter κ for three energies (0.1, 1, 6 keV). (i–j): Defense Meteorological Satellite Program (DMSP)-F16 ion and electron flux data near the magnetospheric multiscale (MMS) foot point (i) before and (j) during the preconditioning. (k) The location of MMS mapped along empirically modeled (using T96) magnetospheric field lines to their foot points in the southern ionosphere.

In summary, convection was very weak during the preconditioning phase, and the predominance of open-field-line reconnection indicates that significant day-to-night flux transport is not expected.

3.4. Polar Cap During Preconditioning: Simulation

We compare with our global MHD simulation to verify the picture of the weakly forward or reverse polar cap convection. Before $\Delta P_{\mathrm{dyn},1}$ impacted the simulated magnetosphere, reverse sunward convection was observed in the simulated polar ionosphere (not pictured), indicative of open-field-line reconnection poleward of the cusps. This is consistent with expectations based on the measured PCN index (Figure 5a). Very weak <0.5 km/s dawn-dusk asymmetric noon-to-midnight convection across the polar cap is observed in the simulated northern hemisphere shortly after the $\Delta P_{\mathrm{dyn},1}$ impact, indicative of low-latitude closed-field-line reconnection (Figures 5b and 5c). Much weaker flows across the PCN are observed later in the simulation, prior to the impact of the second pressure pulse (Figures 5f and 5g). Convection in the southern hemisphere is mostly observed in a single-cell pattern around the polar cap boundary (Figures 5d, 5e, 5h, and 5i), particularly in the latter portion of the preconditioning phase, indicating the predominance of open-field-line magnetopause reconnection for a strong IMF $B_Y < 0$ (Reiff & Burch, 1985). The lowest latitude of the simulated PCN boundary expanded equator-ward by over 5° between 4:00 and 5:00 UT (thick black lines, Figures 5b and 5d), which is quantitatively inconsistent with the 2° equator-ward expansion determined from SuperDARN (pink dashed line, Figure 2g). The equator-ward growth of the polar cap boundary indicates loading of opened field lines from the dayside to nightside.

In summary, the MHD model and data agree that weak convection occurred during the preconditioning phase, which was dominated by a single-cell-type motion driven by open-field-line reconnection. While the simulated flux transfer rate was weak, as is also evidenced by the data, the simulated rate was likely overestimated.

3.5. Magnetotail Dynamics During Preconditioning

Given the weak solar wind driving, weak or suppressed low-latitude reconnection rate, and the lack of evidence for significant day-to-nightside flux transport at high latitudes, it is perhaps surprising to see the dramatic transformation of the magnetotail current sheet that took place during the preconditioning phase (Figures 2j–2p). This juxtaposition motivated the layout of Figure 2; the stretching (Figure 2k), thinning (Figure 2l), and intensification (Figure 2m) of the cross-tail current sheet are observed during the first dynamic pressure pulse and as the dynamic pressure subsided, in the absence of any discernible external driver. The thinning of the current sheet is also visible in the growth of ion thermal pressure nongyrotropy (Figure 2o), which grew to a few percent prior to the arrival of $\Delta P_{\mathrm{dyn},2}$, indicating that the current sheet was thin enough to support meandering ion motions (Zenitani & Nagai, 2016). Figures 2a and 2n show that the magnetotail and solar wind pressures evolved in lock step, both increasing by +55% during the passage of $\Delta P_{\mathrm{dyn},1}$, then both decreasing back to their initial values. We interpret this as evidence that the potentially weak flux loading had not substantially altered the magnetopause flaring angle. If the flaring angle had changed significantly, then the tail pressure at the end of preconditioning would have been significantly different from its initial value, given that the initial and final solar wind pressures were very similar.

Still, and regardless of whether the magnetotail was or was not weakly driven by flux loading, we seek to understand how the tail current sheet thickness was reduced by roughly a factor of 5 and the northward equatorial magnetic field was reduced by over two orders of magnitude. The thickness of a Harris current sheet is controlled by the balance of the internal thermal and the external magnetic pressures. From 3:10 to 3:52 UT, the current sheet thinning may be explained by external compression resulting from $\Delta P_{\mathrm{dyn},1} > 0$. What is needed is an explanation for the thinning between 3:52 and 5:14 UT, which occurred while the tail and solar wind pressures decreased.

In the absence of external compression, the thickness of a one-dimensional current sheet can only be reduced by depleting the equatorial thermal pressure. The magnetic flux depletion mechanism of Hsieh and Otto (2015) drives thinning by depleting high-entropy flux tubes from the central plasma sheet. Magnetic flux depletion is manifested as the slow sunward convection of flux tubes, which are then convected in the azimuthal direction near the plasma sheet-dipole boundary region (Sun et al., 2017). This convection, however, is driven by pressure gradients established when the magnetopause is significantly eroded via low-latitude dayside reconnection, which is not observed for this event. This flux depletion mechanism may also be relevant in the near-Earth plasma sheet. Further evidence that this mechanism is not relevant for this event's preconditioning phase is that there is no discernible sunward convection at MMS (Figure 6a).

We also consider the possibility that current sheet was being torqued by high-latitude lobe reconnection, which allows the IMF B_Y to penetrate into the magnetosphere. During the preconditioning, MMS observed consistently dusk-ward B_Y, which is directed oppositely to the dawn-ward IMF B_Y. Thus, we conclude that the high-latitude reconnection did not significantly impact the tail geometry at the MMS location.

Nonadiabatic particle meandering can move particles—particularly high-energy ions, which contribute to the internal current sheet thermal pressure—across flux tubes. Duskward ion velocities of 20–30 km/s, faster than the $\vec{E} \times \vec{B}$-drift velocity, are observed by MMS during the preconditioning (Figure 6b). These duskward-moving ions are not correlated with significant pressure nongyrotropies, however, indicating that they are likely diamagnetic motions, which do not drive particle transport. Thus meandering-driven thermal pressure loss does not likely explain the current sheet thinning.

Lastly, we note the presence of small but persistent field-aligned ion and electron bulk velocities between $-20 \lesssim V_{\parallel} \lesssim 0$ km/s (Figure 6c). These very small bulk velocities are carried predominantly by fast-moving thermal ions with energies greater than $\gtrsim$6 keV (Figure 6f), and their earthward motion out of the plasma sheet is visible as a moderate heat flux ($0 \gtrsim H_{i\parallel} \gtrsim -20$ nPa·km/s; Figure 6g). The departure of the $\gtrsim$6 keV ions may constitute a substantial net loss of thermal energy from the plasma sheet as, early in the preconditioning phase, these high-energy ions contributed significantly to the bulk thermal pressure (Figure 6e). The non-zero heat flux also indicates a violation of entropy conservation in the plasma sheet at MMS (though strictly speaking this requires a nonzero $\nabla \cdot \vec{H}$). Nonadiabatic evolution of the current sheet and the breakdown of entropy conservation is understood to be a critical step toward enabling instability growth, for example, ballooning and flux transport (Birn et al., 2009). If these ions are truly lost from the plasma sheet, for instance, if they have been pitch angle-scattered into the loss cone and are lost to the neutral atmosphere, then the plasma sheet volume must decrease (i.e., thinning) to preserve pressure equilibrium with the lobes and shocked solar wind. The analogy, again, is like letting air out of a balloon to deflate it (or, slightly more accurately but less common in practice, putting the balloon in a refrigerator and letting the atmosphere compress it).

Figures 6h–6k investigate whether the ions are indeed pitch angle scattered into the loss cone by (a) examining whether the plasma sheet conditions favor scattering and (b) examining particle fluxes in the ionosphere at the MMS foot point. Typically, the threshold $\kappa \leq 3$ (see introduction) is used to identify when pitch angle scattering is enabled. The curvature parameter κ is calculated for 0.1, 1, and 6 keV protons in Figure 6h. The current sheet thickness was too large during this stage of preconditioning to be resolved by the electron-scale MMS tetrahedron, so R_c is calculated as $R_c \approx hB_z/B_0$, as in Büchner and Zelenyi (1989; Equation 4). As is demonstrated in Figure 6h, $\kappa \lesssim 3$ was reached for 6 keV protons during the initial solar-wind-driven compression (interval between the first two vertical lines in Figure 6h). κ continued decreasing as the solar wind dynamic pressure abated (between the second and third vertical dashed lines). As κ became smaller than 1, that is, the curvature radius became much smaller than the gyroradius, MMS observed a steady increase in the ion pressure nongyrotropy, which is consistent with ordered nonadiabatic meandering ion motions, as expected for $\kappa \ll 1$. As the plasma sheet κ transitioned from the pitch angle scattering regime to the meandering orbit regime, MMS observed a reduction or cessation in the net Earthward flow of ions (Figures 6c and 6f).

DMSP F-16 crossed the ionosphere at high southern latitudes near the MMS foot point (Figure 6k) twice during the interval of Figure 6. Comparing the crossings before (Figure 6i) and during preconditioning (Figure 6j) indicates that downward fluxes of ions with plasma sheet-like energies (~hundreds eV to several keV) increased by up to two orders of magnitude during preconditioning.

In summary, we conclude that (a) increased pitch angle scattering removed high-energy thermal protons from the central plasma sheet by scattering them into the loss cone, and (b) this “lost” population had contributed significantly to the plasma sheet thermal pressure at the start of the preconditioning phase. It is possible that this scattering-driven proton loss contributed to (rather than resulted from) current sheet thinning, with a simple analogy being drawn to letting the air out of a balloon (though in our case, the loss of thermal energy rather than number density is likely more relevant). More theoretical work is needed to evaluate whether this precipitative loss of particles can substantially thin the plasma sheet. While scattering-driven losses of hot ions likely contribute to the correlation between current sheet stretching ($\partial B_Z/\partial t < 0$) and plasma sheet cooling (see Runov et al., 2021 and references therein); however, the temperature decrease is typically associated with the influx of cold ions from the ionosphere and flanks (Artemyev et al., 2019). Note, however, given that flux loading at high latitudes and flux tube depletion at low latitudes are not operating in any discernible capacity, it is not clear how else the plasma sheet may have become thin during the preconditioning phase.

3.6. Impact of Second Solar Wind Pressure Pulse and Reconnection

By 5:08 UT, the cross-tail current sheet had been thinned substantially and the north–south component of the plasma sheet magnetic field had been reduced nearly to zero; that is, the conditions that had given stability to the magnetotail current sheet had been eroded. At 5:08 UT, ACE detected a second smaller transient pulse in the solar wind dynamic pressure (second vertical dashed line, Figure 2a). Upon the arrival of the pulse, the magnetotail current sheet evolved rapidly. The half-thickness collapsed below the ion inertial scale (roughly 0.1–0.2 R_E at 5:08 UT). Low and then high-frequency flapping-mode waves were observed (Figure 2j). The north–south component of the plasma sheet magnetic field ceased its monotonic approach toward 0 nT and became highly structured, with strong positive and negative values being observed shortly after the current sheet collapse began (Figure 2k). The magnetotail total pressure—rather than rising with the solar wind dynamic pressure—began a precipitous fall (Figure 2n). MMS also observed an explosive growth of the ion nongyrotropy (Figure 2o). Lastly, near 5:10 UT, MMS observed the growth and then reversal of a fast ion jet (Figure 2p), characteristic of reconnection.

The importance of the preconditioning is evidenced by the fact that the first larger solar wind pressure pulse did not trigger reconnection while the second pulse did. Based on the nearly simultaneous timing of the solar wind pressure pulse arrival, the current sheet collapse, and the reconnection onset, we conclude that the deformation of the current sheet boundary conditions by the deformation of the high-latitude magnetotail by the solar wind pressure pulse precipitated the loss of current sheet equilibrium and reconnection onset, as has previously been suggested (Birn et al., 2004; Birn & Schindler, 2002). The companion study, paper 2, investigates the interval near reconnection onset in greater detail.

The reconnection was ultimately short-lived, with the *X*-line being ejected tail-ward immediately after onset, and the recovery of the current sheet thickness began nearly immediately after reconnection onset (Figure 2l). The reconnection also had a negligible impact on the inner magnetosphere. Geosynchronous satellites did not observe any discernible increase in energetic particle fluxes in the minutes after the onset (not pictured). A very weak deflection of the auroral electrojet (AE), a proxy for substorm activity, to −50 nT was the only discernible global signature of the reconnection (see paper 2). The lack of global substorm activity is also evidenced by the absence of this 3 July 2017 5:20 UT event from commonly used substorm lists based on multiple disparate sets of criteria for defining a substorm (Forsyth et al., 2015; Newell & Gjerloev, 2011; Ohtani & Gjerloev, 2020).

4. Summary, Conclusions, and Open Questions

We investigated the global solar wind-magnetospheric interaction that lead to the initiation of magnetotail reconnection during an otherwise quiet interval on 3 July 2017. ACE data from the upstream solar wind identified two transient solar wind pressure pulses as the likely drivers of MMS-observed magnetotail dynamics. THEMIS-D and E data demonstrated the lack of any significant low-latitude magnetopause reconnection signatures, with the possible exception being two ∼50 km/s plasma flows near 5:10 UT, both observed by THEMIS-D. THEMIS-E, which was lower in altitude than THEMIS-D, observed a significant compression of the magnetopause after the arrival of the first solar wind pressure pulse, which also leads to a 4-fold increase in the magnetosheath density at THEMIS-D. Based on the modeled and observed magnetopause shear angle and the observed magnetopause $\Delta\beta$, we concluded that magnetopause reconnection may have been suppressed at low latitudes. This conclusion was consistent with (a) AMPERE data, which showed no or very weak FACs at the low-latitude dayside magnetopause, and (b) the SuperDARN-derived cross-polar-cap potential and convection boundary location, both of which indicated that convection and flux loading were either not occurring or very weak. A global MHD simulation was investigated to verify the weakly driven nature of the polar cap.

MMS observations indicated that the first solar wind pressure pulse triggered the gradual thinning and stretching of the cross-tail current sheet, which continued as the solar wind pressure abated. We suggested a new mechanism to explain this thinning; namely, the evacuation of the plasma sheet thermal pressure by pitch angle scattering and precipitation. Pitch angle scattering and precipitation were both apparently active, as observed by MMS and DMSP F-16, respectively. The plausibility of this mechanism for thinning the current sheet was not evaluated from a quantitative and theoretical perspective. Regardless of the cause, we demonstrate that substantial deformation and destabilization of the cross-tail current sheet is possible with the absence of strong solar wind driving by southward IMF. Finally, we point out the importance of the preconditioning interval is demonstrated that the two identical solar wind drivers (two pressure pulses) elicited dramatically different responses before and after the current sheet thinning.

There are many open questions raised by this work. Since we do not have access to auroral images given as this event took place near the northern summer solstice: (a) what, if any, are the auroral signatures of this type of quiescent magnetotail reconnection? (b) Is this a truly viable mechanism for current sheet thinning, and if so then does it play a role in more intense substorms? (c) Why did this reconnection event not trigger a substorm, and (d) why were there no energetic particle injections observed at geosynchronous orbit? Only a fraction of these questions may be answerable with the present heliophysics system observatory.

Data Availability Statement

MMS data, including FGM (Russell et al., 2022), FPI (Gershman et al., 2022a, 2022b), and EIS (Cohen et al., 2022a, 2022b), were obtained from https://lasp.colorado.edu/mms/sdc/public. DMSP data were obtained from https://dmsp.bc.edu. THEMIS ESA (McFadden et al., 2008) and FGM (Auster et al., 2008) data were obtained from http://themis.ssl.berkeley.edu. AMPERE data (Waters et al., 2020) were obtained from https://ampere.jhuapl.edu/. SuperDARN data were obtained from http://vt.superdarn.org. ACE data were obtained from https://cdaweb.gsfc.nasa.gov. Substorm event lists are maintained by SuperMAG and are available at https://supermag.jhuapl.edu/substorms/. LANL SOPA data are not publicly available, and can be obtained for limited case studies by inquiry to the SOPA team (see https://cdaweb.gsfc.nasa.gov/Recent_LANL_Data.html). The Space Physics Environment Data Analysis System (SPEDAS) software package (Angelopoulos et al., 2019) was used.

Acknowledgments

KJG, CJF, and RBT were supported by NASA's MMS FIELDS contract NNG04EB99C. We acknowledge NASA contract NAS5-02099 and V. Angelopoulos for use of data from the THEMIS Mission. We acknowledge the contributions made by many to collect and distribute the data sets used in this study.

References

Akasofu, S. I. (1981). Energy coupling between the solar wind and the magnetosphere. *Space Science Reviews*, *28*(2), 121–190. https://doi.org/10.1007/BF00218810

Angelopoulos, V. (2008). The THEMIS Mission. *Space Science Reviews*, *141*(1), 5–34. https://doi.org/10.1007/s11214-008-9336-1

Angelopoulos, V., Cruce, P., Drozdov, A., Grimes, E. W., Hatzigeorgiu, N., King, D. A., et al. (2019). The Space Physics Environment Data Analysis System (SPEDAS). *Space Science Reviews*, *215*(1), 9. https://doi.org/10.1007/s11214-018-0576-4

Artemyev, A. V., Angelopoulos, V., Runov, A., & Petrukovich, A. A. (2019). Global view of current sheet thinning: Plasma pressure gradients and large-scale currents. *Journal of Geophysical Research: Space Physics*, *124*(1), 264–278. https://doi.org/10.1029/2018JA026113

Auster, H. U., Glassmeier, K. H., Magnes, W., Aydogar, O., Baumjohann, W., Constantinescu, D., et al. (2008). The THEMIS fluxgate magnetometer. *Space Science Reviews*, *141*(1–4), 235–264. https://doi.org/10.1007/s11214-008-9365-9

Baker, D. N., Pulkkinen, T. I., Angelopoulos, V., Baumjohann, W., & McPherron, R. L. (1996). Neutral line model of substorms: Past results and present view. *Journal of Geophysical Research: Space Physics*, *101*(A6), 12975–13010. https://doi.org/10.1029/95JA03753

Birn, J., Dorelli, J. C., Hesse, M., & Schindler, K. (2004). Thin current sheets and loss of equilibrium: Three-dimensional theory and simulations. *Journal of Geophysical Research: Space Physics*, *109*(A2), A02215. https://doi.org/10.1029/2003JA010275

Birn, J., Hesse, M., Schindler, K., & Zaharia, S. (2009). Role of entropy in magnetotail dynamics. *Journal of Geophysical Research: Space Physics*, *114*(A9), A00D03. https://doi.org/10.1029/2008JA014015

Birn, J., & Schindler, K. (2002). Thin current sheets in the magnetotail and the loss of equilibrium. *Journal of Geophysical Research: Space Physics*, *107*(A7), SMP 18-1–SMP 18-10. https://doi.org/10.1029/2001JA000291

Boyle, C. B., Reiff, P. H., & Hairston, M. R. (1997). Empirical polar cap potentials. *Journal of Geophysical Research: Space Physics*, *102*(A1), 111–125. https://doi.org/10.1029/96JA01742

Büchner, J., & Zelenyi, L. M. (1987). Chaotization of the electron motion as the cause of an internal magnetotail instability and substorm onset. *Journal of Geophysical Research: Space Physics*, *92*(A12), 13456–13466. https://doi.org/10.1029/JA092iA12p13456

Büchner, J., & Zelenyi, L. M. (1989). Regular and chaotic charged particle motion in magnetotaillike field reversals: 1. Basic theory of trapped motion. *Journal of Geophysical Research: Space Physics*, *94*(A9), 11821–11842. https://doi.org/10.1029/JA094iA09p11821

Burch, J. L., Moore, T. E., Torbert, R. B., & Giles, B. L. (2016). Magnetospheric multiscale overview and science objectives. *Space Science Reviews*, *199*(1–4), 5–21. https://doi.org/10.1007/s11214-015-0164-9

Burch, J. L., Reiff, P. H., Menietti, J. D., Heelis, R. A., Hanson, W. B., Shawhan, S. D., et al. (1985). IMF B_y-dependent plasma flow and Birkeland currents in the dayside magnetosphere: 1. Dynamics explorer observations. *Journal of Geophysical Research: Space Physics*, *90*(A2), 1577–1593. https://doi.org/10.1029/JA090iA02p01577

Cohen, I. J., Mauk, B. H., & Burch, J. L. (2022a). MMS 1 Energetic Particle Detector, Energetic Ion Spectrometer (EPD-EIS) Energy by Time of Flight, Level 2 (L2), Burst Mode, 0.605 s Data [Dataset]. NASA Space Physics Data Facility. https://doi.org/10.48322/c8gk-pv81

Cohen, I. J., Mauk, B. H., & Burch, J. L. (2022b). MMS 1 Energetic Particle Detector, Energetic Ion Spectrometer (EPD-EIS) Pulse Height by Time of Flight, Level 2 (L2), Burst Mode, 0.605 s Data [Dataset]. NASA Space Physics Data Facility. https://doi.org/10.48322/f8pf-hj26

Cooling, B. M. A., Owen, C. J., & Schwartz, S. J. (2001). Role of the magnetosheath flow in determining the motion of open flux tubes. *Journal of Geophysical Research: Space Physics*, *106*(A9), 18763–18775. https://doi.org/10.1029/2000JA000455

Coxon, J. C., Milan, S. E., Clausen, L. B. N., Anderson, B. J., & Korth, H. (2014). A superposed epoch analysis of the regions 1 and 2 Birkeland currents observed by AMPERE during substorms. *Journal of Geophysical Research: Space Physics*, *119*(12), 9834–9846. https://doi.org/10.1002/2014JA020500

Crooker, N. U. (1979). Dayside merging and cusp geometry. *Journal of Geophysical Research: Space Physics*, *84*(A3), 951–959. https://doi.org/10.1029/JA084iA03p00951

Delcourt, D. C., Sauvaud, J.-A., Martin, R. F., Jr., & Moore, T. E. (1996). On the nonadiabatic precipitation of ions from the near-Earth plasma sheet. *Journal of Geophysical Research: Space Physics*, *101*(A8), 17409–17418. https://doi.org/10.1029/96JA01006

Donovan, E., Spanswick, E., Liang, J., Grant, J., Jackel, B., & Greffen, M. (2012). Magnetospheric dynamics and the proton aurora. *Auroral phenomenology and magnetospheric processes: Earth and other planets* (pp. 365–378). American Geophysical Union (AGU). https://doi.org/10.1029/2012GM001241

Dungey, J. W. (1961). Interplanetary magnetic field and the auroral zones. *Physical Review Letters*, *6*(2), 47–48. https://doi.org/10.1103/PhysRevLett.6.47

Forsyth, C., Rae, I. J., Coxon, J. C., Freeman, M. P., Jackman, C. M., Gjerloev, J., & Fazakerley, A. N. (2015). A new technique for determining Substorm Onsets and Phases from Indices of the Electrojet (SOPHIE). *Journal of Geophysical Research: Space Physics*, *120*(12), 10592–10606. https://doi.org/10.1002/2015JA021343

Gershman, D. J., Giles, B. L., Pollock, C. J., Moore, T. E., & Burch, J. L. (2022a). MMS 1 Fast Plasma Investigation, Dual Electron Spectrometer (FPI, DES) Distribution Moments, Level 2 (L2), Burst Mode, 30 ms Data [Dataset]. NASA Space Physics Data Facility. https://doi.org/10.48322/6172-zw20

Gershman, D. J., Giles, B. L., Pollock, C. J., Moore, T. E., & Burch, J. L. (2022b). MMS 1 Fast Plasma Investigation, Dual Ion Spectrometer (FPI, DIS) Distribution Moments, Level 2 (L2), Burst Mode, 0.15 s Data [Dataset]. NASA Space Physics Data Facility. https://doi.org/10.48322/qggf-vr83

Heppner, J. P., & Maynard, N. C. (1987). Empirical high-latitude electric field models. *Journal of Geophysical Research: Space Physics*, *92*(A5), 4467–4489. https://doi.org/10.1029/JA092iA05p04467

Hones, J. E. W. (1979). Transient phenomena in the magnetotail and their relation to substorms. *Space Science Reviews*, *23*(3), 393–410. https://doi.org/10.1007/BF00172247

Hsieh, M.-S., & Otto, A. (2015). Thin current sheet formation in response to the loading and the depletion of magnetic flux during the substorm growth phase. *Journal of Geophysical Research: Space Physics*, *120*(6), 4264–4278. https://doi.org/10.1002/2014JA020925

Imber, S. M., Milan, S. E., & Lester, M. (2013). The Heppner-Maynard Boundary measured by SuperDARN as a proxy for the latitude of the auroral oval. *Journal of Geophysical Research: Space Physics*, *118*(2), 685–697. https://doi.org/10.1029/2012JA018222

Lu, S., Lu, Q., Wang, R., Pritchett, P. L., Hubbert, M., Qi, Y., et al. (2022). Electron-only reconnection as a transition from quiet current sheet to standard reconnection in Earth's magnetotail: Particle-in-cell simulation and application to MMS data. *Geophysical Research Letters*, *49*(11), e2022GL098547. https://doi.org/10.1029/2022GL098547

Lu, S., Wang, R., Lu, Q., Angelopoulos, V., Nakamura, R., Artemyev, A. V., et al. (2020). Magnetotail reconnection onset caused by electron kinetics with a strong external driver. *Nature Communications*, *11*(1), 5049. https://doi.org/10.1038/s41467-020-18787-w

Mauk, B. H., Blake, J. B., Baker, D. N., Clemmons, J. H., Reeves, G. D., Spence, H. E., et al. (2016). The Energetic Particle Detector (EPD) investigation and the Energetic Ion Spectrometer (EIS) for the Magnetospheric Multiscale (MMS) mission. *Space Science Reviews*, *199*(1–4), 471–514. https://doi.org/10.1007/s11214-014-0055-5

McFadden, J. P., Carlson, C. W., Larson, D., Ludlam, M., Abiad, R., Elliott, B., et al. (2008). The THEMIS ESA plasma instrument and in-flight calibration. *Space Science Reviews*, *141*(1–4), 277–302. https://doi.org/10.1007/s11214-008-9440-2

McPherron, R. L., & Hsu, T.-S. (2002). A comparison of substorms occurring during magnetic storms with those occurring during quiet times. *Journal of Geophysical Research: Space Physics*, *107*(A9), SMP 23-1–SMP 23-16. https://doi.org/10.1029/2001JA002008

Newell, P. T., & Gjerloev, J. W. (2011). Evaluation of SuperMAG auroral electrojet indices as indicators of substorms and auroral power. *Journal of Geophysical Research: Space Physics*, *116*(A12), A12211. https://doi.org/10.1029/2011JA016779

Ohtani, S., & Gjerloev, J. W. (2020). Is the substorm current wedge an ensemble of wedgelets?: Revisit to midlatitude positive bays. *Journal of Geophysical Research: Space Physics*, *125*(9), e2020JA027902. https://doi.org/10.1029/2020JA027902

Oliver, W. L., Holt, J. M., Wand, R. H., & Evans, J. V. (1983). Millstone hill incoherent scatter observations of auroral convection over $60° \leq \lambda \leq 75°$: 3. Average patterns versus kp. *Journal of Geophysical Research: Space Physics*, *88*(A7), 5505–5516. https://doi.org/10.1029/JA088iA07p05505

Perreault, P., & Akasofu, S. I. (1978). A study of geomagnetic storms. *Geophysical Journal International*, *54*(3), 547–573. https://doi.org/10.1111/j.1365-246X.1978.tb05494.x

Petrukovich, A., Artemyev, A., Vasko, I., Nakamura, R., & Zelenyi, L. (2015). Current sheets in the Earth magnetotail: Plasma and magnetic field structure with Cluster Project observations. *Space Science Reviews*, *188*(1–4), 311–337. https://doi.org/10.1007/s11214-014-0126-7

Phan, T. D., Paschmann, G., Gosling, J. T., Oieroset, M., Fujimoto, M., Drake, J. F., & Angelopoulos, V. (2013). The dependence of magnetic reconnection on plasma β and magnetic shear: Evidence from magnetopause observations. *Geophysical Research Letters*, *40*(1), 11–16. https://doi.org/10.1029/2012GL054528

Pollock, C., Moore, T., Jacques, A., Burch, J., Gliese, U., Saito, Y., et al. (2016). Fast plasma investigation for magnetospheric multiscale. *Space Science Reviews*, *199*(1–4), 331–406. https://doi.org/10.1007/s11214-016-0245-4

Reiff, P. H., & Burch, J. L. (1985). IMF B_y-dependent plasma flow and Birkeland currents in the dayside magnetosphere: 2. A global model for northward and southward IMF. *Journal of Geophysical Research: Space Physics*, *90*(A2), 1595–1609. https://doi.org/10.1029/JA090iA02p01595

Runov, A., Angelopoulos, V., Artemyev, A., Weygand, J., Lu, S., Lin, Y., & Zhang, X.-J. (2021). Global and local processes of thin current sheet formation during substorm growth phase. *Journal of Atmospheric and Solar-Terrestrial Physics*, *220*, 105671. https://doi.org/10.1016/j.jastp.2021.105671

Russell, C. T., Magnes, W., Wei, H., Bromund, K. R., Plaschke, F., Fischer, D., et al. (2022). MMS 1 Flux Gate Magnetometer (FGM) DC Magnetic Field, Level 2 (L2), Burst Mode, 128 Sample/s, v4/5 [Dataset]. NASA Space Physics Data Facility. https://doi.org/10.48322/pj0n-m695

Sarris, E. T., Krimigis, S. M., & Armstrong, T. P. (1976). Observations of magnetospheric bursts of high-energy protons and electrons at 35 R_E with Imp 7. *Journal of Geophysical Research*, *81*(13), 2341–2355. https://doi.org/10.1029/JA081i013p02341

Sergeev, V., Sazhina, E., Tsyganenko, N., Lundblad, J., & Søraas, F. (1983). Pitch-angle scattering of energetic protons in the magnetotail current sheet as the dominant source of their isotropic precipitation into the nightside ionosphere. *Planetary and Space Science*, *31*(10), 1147–1155. https://doi.org/10.1016/0032-0633(83)90103-4

Sun, W. J., Fu, S. Y., Wei, Y., Yao, Z. H., Rong, Z. J., Zhou, X. Z., et al. (2017). Plasma sheet pressure variations in the near-Earth magnetotail during substorm growth phase: THEMIS observations. *Journal of Geophysical Research: Space Physics*, *122*(12), 12212–12228. https://doi.org/10.1002/2017JA024603

Swisdak, M., Rogers, B. N., Drake, J. F., & Shay, M. A. (2003). Diamagnetic suppression of component magnetic reconnection at the magnetopause. *Journal of Geophysical Research: Space Physics*, *108*(A5), 1218. https://doi.org/10.1029/2002JA009726

Thompson, S. M., Kivelson, M. G., Khurana, K. K., McPherron, R. L., Weygand, J. M., Balogh, A., et al. (2005). Dynamic Harris current sheet thickness from cluster current density and plasma measurements. *Journal of Geophysical Research: Space Physics*, *110*(A2), A02212. https://doi.org/10.1029/2004JA010714

Torbert, R. B., Russell, C. T., Magnes, W., Ergun, R. E., Lindqvist, P.-A., LeContel, O., et al. (2016). The FIELDS instrument suite on MMS: Scientific objectives, measurements, and data products. *Space Science Reviews*, *199*(1–4), 105–135. https://doi.org/10.1007/s11214-014-0109-8

Tóth, G., van der Holst, B., Sokolov, I. V., De Zeeuw, D. L., Gombosi, T. I., Fang, F., et al. (2012). Adaptive numerical algorithms in space weather modeling. *Journal of Computational Physics*, *231*(3), 870–903. https://doi.org/10.1016/j.jcp.2011.02.006

Trattner, K. J., Mulcock, J. S., Petrinec, S. M., & Fuselier, S. A. (2007). Location of the reconnection line at the magnetopause during southward IMF conditions. *Geophysical Research Letters*, *34*(3), L03108. https://doi.org/10.1029/2006GL028397

Troshichev, O., Andrezen, V., Vennerstrøm, S., & Friis-Christensen, E. (1988). Magnetic activity in the polar cap—A new index. *Planetary and Space Science*, *36*(11), 1095–1102. https://doi.org/10.1016/0032-0633(88)90063-3

Tsyganenko, N. A. (1995). Modeling the Earth's magnetospheric magnetic field confined within a realistic magnetopause. *Journal of Geophysical Research: Space Physics*, *100*(A4), 5599–5612. https://doi.org/10.1029/94JA03193

Tsyganenko, N. A. (1996). Effects of the solar wind conditions in the global magnetospheric configurations as deduced from data-based field models (Invited). In E. J. Rolfe & B. Kaldeich (Eds.), *International Conference on Substorms* (Vol. 389, p. 181).

Tsyganenko, N. A., & Sitnov, M. I. (2007). Magnetospheric configurations from a high-resolution data-based magnetic field model. *Journal of Geophysical Research: Space Physics*, *112*(A6), A06225. https://doi.org/10.1029/2007JA012260

Waters, C. L., Anderson, B. J., Green, D. L., Korth, H., Barnes, R. J., & Vanhamäki, H. (2020). Science data products for ampere. In M. W. Dunlop & H. Lühr (Eds.), *Ionospheric multi-spacecraft analysis tools: Approaches for deriving ionospheric parameters* (pp. 141–165). Springer International Publishing. https://doi.org/10.1007/978-3-030-26732-2_7

Zenitani, S., & Nagai, T. (2016). Particle dynamics in the electron current layer in collisionless magnetic reconnection. *Physics of Plasmas*, *23*(10), 102102. https://doi.org/10.1063/1.4963008

Zhang, L. Q., Baumjohann, W., Wang, C., Dai, L., & Tang, B. B. (2016). Bursty bulk flows at different magnetospheric activity levels: Dependence on IMF conditions. *Journal of Geophysical Research: Space Physics*, *121*(9), 8773–8789. https://doi.org/10.1002/2016JA022397